**Title:**

# Deep mapping of the *endomembrane system* of cerebellar Purkinje neurons

**Authors**

Matthias G Haberl[1,2,3,*], Silvia Viana da Silva[4,5], Sebastien Phan[1,2], Eric Bushong[1,2], Thomas Deerinck[1,2], Mark H Ellisman[1,2,*]

[1]Department of Neurosciences, UCSD, La Jolla, CA; [2]National Center for Microscopy and Imaging Research (NCMIR), UCSD, La Jolla, CA [3]Current Affiliation: Neurowissenschaftliches Forschungszentrum, Charité Universitätsmedizin, Berlin, Germany [4]DZNE, Berlin, Germany [5]Division of Biolological Science, Neurobiology, UCSD, La Jolla, CA

*Correspondence to: matthias.haberl@charite.de and mellisman@ucsd.edu

## Summary

Neuronal function relies on the precise spatial organization of intracellular membrane-bounded organelles involved in anabolism and $Ca^{2+}$ sequestration, such as the Golgi apparatus, mitochondria and the endoplasmic reticulum (ER), along with structures involved in catabolism, such as lysosomes. Despite their known roles in energy supply, calcium homeostasis, and proteostasis, our understanding of how the anabolism-linked organelles are structurally arranged within neurons remains incomplete. Due to the tremendous complexity in the morphologies and fine structural features and interwoven nature of these intracellular organelles, particularly the ER, our understanding of their structural organization is limited, particularly, with regard to quantitative assessments of their sites of interaction and accurate measures of their volumetric proportions inside of a single large neuron. To approach this challenge, we used serial block-face scanning electron microscopy (SBEM) to generate large-scale 3D EM volumes and electron tomography on high-pressure frozen tissue of the rodent cerebellum, including the largest cells in the vertebrate brain, the cerebellar Purkinje neuron as well as the most abundant cell type in the vertebrate brain, the much smaller cerebellar granule neuron. We reconstructed the neuronal ultrastructure of these different cell types, focusing on the ER, mitochondria and membrane contact sites, to then characterize intracellular motifs and organization principles in detail, providing a first full map to quantitatively describe a neuronal *endoarchitectome*. At the gross level organization, we found that the intracellular composite of organelles are cell type specific features, with specific differences between Purkinje neurons and Granule cells. At the level of fine structure, we

mapped ultrastructural domains within Purkinje neurons where ER and mitochondria associate directly. In addition to cell type specific differences, we observed significant subcellular regional variation, particularly within the axon initial segment (AIS) of Purkinje neurons, where we identified ultrastructural domains with sharply contrasting distributions of ER and mitochondria. These findings suggest a finely tuned spatial organization of organelles that may underpin the distinct functional demands along the axon. We expect that our subcellular map, along with the methods developed to obtain these maps, will facilitate future studies in health, aging and disease to characterize defined features, by developing a framework for quantitative analysis of the neuronal ultrastructure.

## Introduction

The endoplasmic reticulum (ER) in neurons is a large and complex organelle, which starting from the nuclear envelope (*1*) meanders throughout soma, axons (*2*, *3*) and dendrites, and even into the presynaptic boutons (*4*) and postsynaptic spines (*5*, *6*). The ER is linked with the Golgi apparatus (*7*) and has numerous contact sites with the cell membrane and mitochondria (*8*, *9*) which are critical for its function in regulating intracellular calcium. To this end, it has a lumen rich in sequestered $Ca^{2+}$ (*2*), which is released through its membrane by $Ca^{2+}$ channels, specifically inositol trisphosphate receptors (IP3Rs) and ryanodine receptors (*10*). Within the soma of neurons, the ER is a major constituent in volume and surface, yet it has received much less attention compared to the much smaller, less prominent ER in spines, referred to as spine apparatus (see e.g. (*6*, *11*) and reviewed in (*12*)), since its dimensions are difficult capture and reconstruct at sufficient resolution it poses a tremendous problem for segmentation at scale. Anatomically there are a few broadly defined configurations of ER in cells and neurons, besides the nuclear envelope, namely sheets and tubules (*13*, *14*). Even though we know that also local domains can influence $Ca^{2+}$-signals (*15*), the precise three-dimensional distribution of the ER and the occurrence of intracellular motifs in neurons from brain tissue have so far been difficult to quantify.

To address these questions about the ultrastructural organization in neurons, we acquired high-resolution multi-tilt tomograms and serial block-face scanning electron microscopic (SBEM) volumes (*16*) of cerebellar tissue. We then performed large-scale 3D reconstructions of the cellular constituents including mitochondria and the endoplasmic reticulum of granule cells and Purkinje neurons. These two cell types represent extremes in neuronal architecture, with granule cells among the smallest, and Purkinje neurons among the largest and most morphologically complex in the brain. Notably, the Purkinje neuron is a prominent inhibitory interneuron whose physiology, gene expression, and role within neural circuits have been extensively characterized across vertebrate species and throughout evolution. Based on our 3D segmentations, we performed quantifications of the intracellular architecture of Purkinje

neuron somata and the axon initial segment (AIS). We then characterized in detail the intracellular ultrastructure of the neuronal soma of Purkinje neurons, which are large GABAergic inhibitory neurons, providing the sole output of motor coordination from the cerebellar cortex (*17*).

Intracellular morphological organization principles of neurons are critical to understand spatial constraints imposed on intracellular functions and intracellular signaling traveling of messenger molecules that are important for the communication in the brain. Large-scale volume electron microscopy (vEM) is rapidly becoming widely used to obtain dense connectomic reconstructions across species, brain regions and physiological states (*18–23*). Similarly whole-cell organelle segmentations of these vEM data are being carried out on cultured cells or assemblies of cells in somatic organs, like those of pancreatic islets, at larger scales (*24–26*), propelled by advances in deep learning, computational resource growth and AI. The work described here demonstrates the application of these strategies and lays out a foundation for future studies with examples of quantifiable parameters relevant to the intracellular organization, in particular for neuronal somata, axons and dendrites in health and disease. We expect that our work thus provides a first ultrastructural blueprint of a neuronal *endoarchitectome*, which provides detailed information required for computational spatial simulations and can contribute to a next level of cell type characterizations, across ages, during dynamics of activities and variations in underlying health.

## Results

### Large- and fine-scale reconstructions of the 3D intracellular ultrastructure of the cerebellar cell somata from volumetric electron microscopy datasets

Reconstructing the intracellular features of neuronal somata, such as the endoplasmic reticulum and mitochondria, is a multiscale problem spanning from the few nm-scale of the ER diameter to tens of µm to capture the profile of intracellular distributions. In order to generate large-scale 3D maps of the ultrastructural features of Purkinje neuron somata we used serial block-face scanning electron microscopy (SBEM) of *en-bloc* stained mouse cerebellar cortex tissue for large-scale measurements to EM volumes (**Figure 1**). We acquired two SBEM microscopy datasets: one from the cerebellum of an adult male mouse with a size of $57.17 \times 76.22 \times 17\ \mu m^3$ where we segmented the cellular ultrastructure of Purkinje neurons (**Figure 1 b-e**) and granule cells (**Figure 1 f-h**) and one dataset from the cerebellum of an adult rat with a size of $189 \times 118 \times 60\ \mu m^3$, which includes the axon initial segment. The subsequent 3D segmentations of the electron microscopic data volumes were performed by training deep neural networks models with CDeep3M (*27*) for segmenting different cellular structures and subsequent manual proof editing of the computational segmentations by expert annotators. In order to gain insights about cell type dependent variation of the intracellular composition, we

111 first analyzed the volume of soma, nuclei, cytoplasm ER and mitochondria in Purkinje neurons
112 (**Figure 1i**) and granule cells (**Figure 1j**) based on the proof-edited SBEM segmentations.
113 When calculating the respective somatic volume fraction occupancy by ER and mitochondria,
114 we found that even though a Purkinje neuron has ~80 times more mitochondria (i.e. >2700
115 versus 34 ± 5) than a granule cell, the relative volume fraction occupied by mitochondria was
116 similar in between Purkinje (9.4%) and granule cells (10,0 ± 1,1%) in the same imaging volume
117 (**Figure 1k**). Whereas a comparison of ER occupancy revealed that the ER occupied 12.3% in
118 the Purkinje, but only 5,8 ± 0,9 % in the granule cells (**Figure 1l**).
119 In order to support our analysis of fine-scale intracellular structural features at higher
120 resolution, we also acquired multi-tilt electron tomography datasets of high-pressure frozen,
121 freeze substituted tissue, of cerebellar mouse cortex, a technique which can be scaled to
122 perform large scale high resolution connectomics (*28*).
123 We acquired, segmented and reconstructed five three-dimensional, high-resolution, multi-tilt
124 electron tomography volumes, at the dendritic and the axonal poles of cerebellar Purkinje
125 neurons (**Figure 2 a-c**). The electron tomography volumes were acquired from following areas:
126 Volume 1, 2 and 3 were acquired at the dendritic pole of Purkinje neurons in the mouse
127 cerebellum, Volume 4 and 5 were acquired at the axonal pole of Purkinje neurons in the mouse
128 cerebellum (**Supplementary Figure 1**).

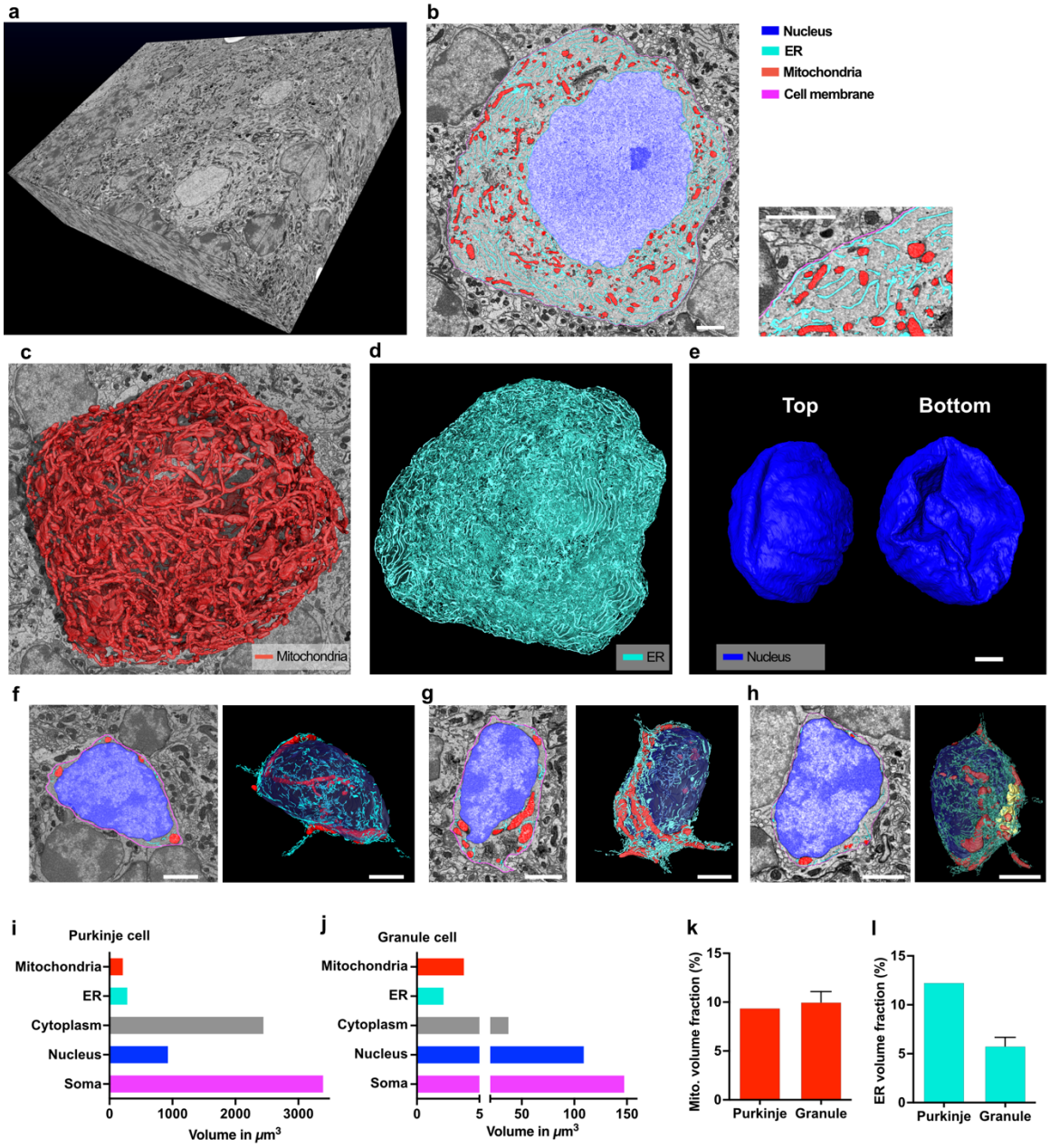


**Figure 1. Large-scale 3D reconstructions of the intracellular ultrastructure of cerebellar Purkinje neurons and granule cells.** Individual 2D view of (**a**) electron tomogram of Purkinje neuron soma acquired from high-pressure frozen freeze substituted cerebellar tissue. (**b**) Intracellular structures including the endoplasmic reticulum were computationally segmented and manually proof edited before quantifications. (**c**) Overlay in 2D of the tomogram displaying segmentations of the ER (cyan), mitochondria (red), nucleus (blue), golgi apparatus (yellow). (**d**) Overlay of 3D surface meshes of these intracellular structures and the cell membrane from one electron tomography volume. (**e**) Volume view of serial block-face scanning electron microscopy, performed on an *en-bloc* stained cerebellar tissue containing Purkinje neurons and granule cells. Example 2D planes of (**f**) Purkinje neuron soma and (**g**) granule cell soma, both overlayed with ER (cyan), mitochondria (red), nucleus (blue) and cell membrane (yellow) segmentations. 3D surface meshes of the Purkinje neuron (**h**) mitochondria (red) and (**i**) ER (cyan). Quantification of the absolute volume of the segmented organelles for the (**j**) Purkinje neuron soma and (**k**) granule cell soma. Direct comparison of the volume fractions of intracellular structures of Purkinje neurons and granule cell soma shows (**l**) similarity in mitochondria content and (**m**) a large difference in the ER content between the two cell types. Scale Bars (b-h): 2μm

129

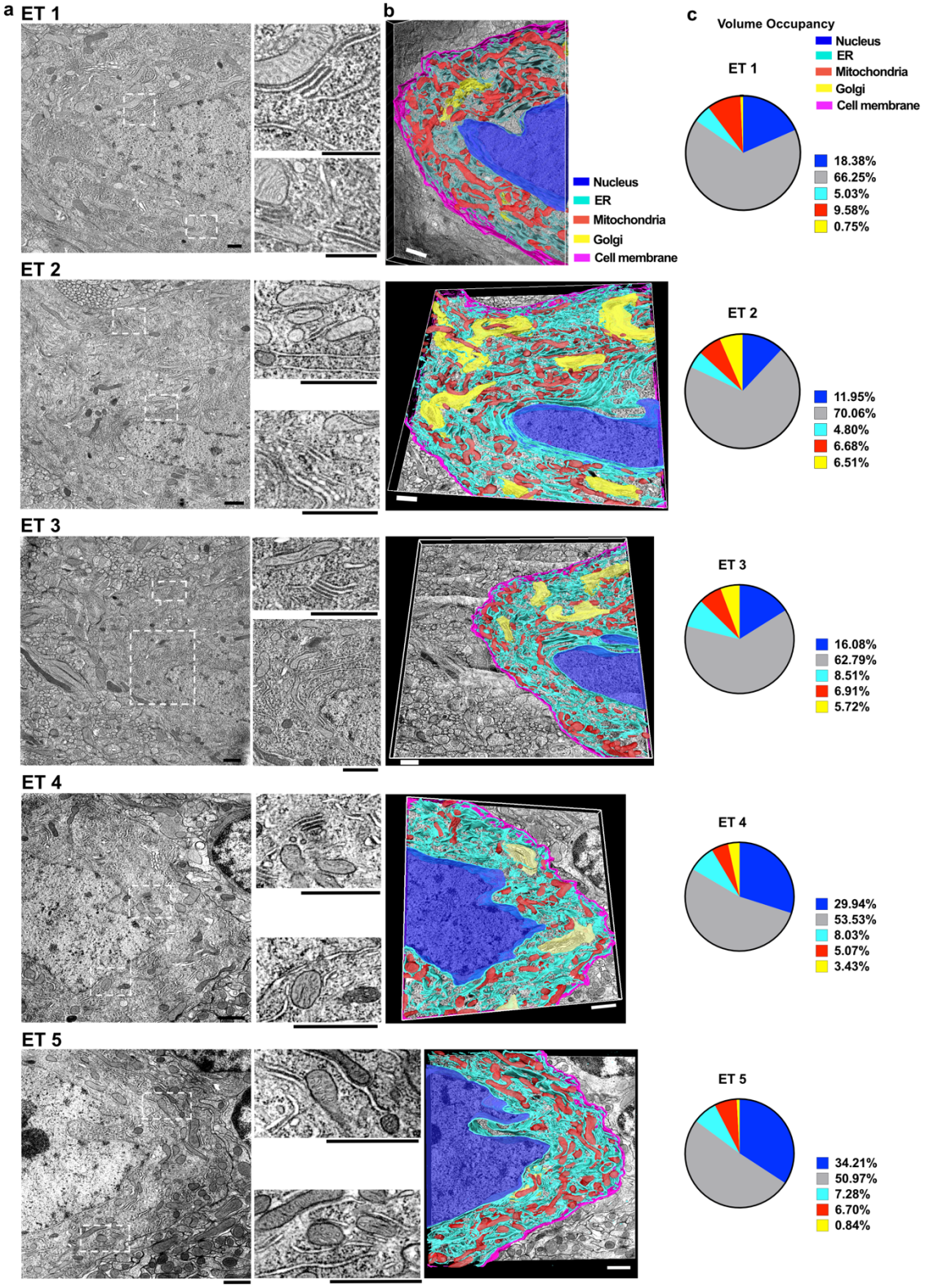


**Figure 2. Segmentation of the intracellular architecture of Purkinje neurons based on five semi-thick electron tomography volumes.** (**a**) 2D views from electron tomography volumes (ET 1-5) of Purkinje neuron soma acquired from high-pressure frozen freeze substituted cerebellar tissue. Based on these the intracellular structures including the endoplasmic reticulum were computationally segmented and manually proof edited before quantifications. (**b**) Overlay of 3D surface meshes based on segmentations of the cell membrane (magenta), ER (cyan), mitochondria (red), nucleus (blue), Golgi apparatus (yellow) showing the intracellular arrangement in the electron tomography volumes. (**c**) Volume occupancy ratios within the Purkinje neuron in each of the electron tomography volumes of intracellular organelles: nucleus, ER, mitochondria and Golgi apparatus. Cytoplasm volume was calculated as volume enclosed by the cell membrane without the volume of nucleus, ER, mitochondria and Golgi apparatus. Scale Bars: 1µm

**Somatic ER of Purkinje neurons is omnipresent and also oriented perpendicular to the plasma membrane**

To characterize the morphological features of the ER, we first performed automated measurements on the reconstructions of the SBEM data where we find an average ER diameter of 44.09nm ± 12.39 nm (**Figure 3a**), which is in line with results from our high-resolution tomography data (average ER diameter of 39.25 nm ± 10.55 nm; **Supplementary Figure 2**), and an average length of in plane ER strands of 426.8 nm ± 580.5 nm (**Figure 3b**). Interestingly, we find a significant proportion of the somatic ER in the Purkinje neuron falls in the category of narrow ER (e.g. 26.9% 20-30nm in ET2; **Supplementary Figure 2**), which was suggested to be a property of axonal ER only recently (*29*).

Since the ER has several critical roles in the neuronal signaling, we wanted to determine if this implies that the structure is well distributed throughout the entire soma (excluding the interior of the nucleus), or if areas with little or no ER exist. Performing a distance analysis (heatmap plotted in **Figure 3c**), we found that indeed nearly all of the soma has ER within a distance of 250nm (93.44% of soma area has ER within 250nm and 99.37% of soma area has ER within 500nm) (**Figure 3d**). In summary, this means that ER is omnipresent throughout the soma of the Purkinje neurons and nearly all areas in the soma have ER within a short distance, underlining its critical role for cellular processes.

Since we found that the ER is omnipresent throughout the neuronal soma, we wanted to test if this also entails that it is uniformly distributed. Therefore, we performed a radial analysis of ER-occupancy (normalized by the volume at each distance). We found that the most dominant feature in this radial distribution is a prominent occupancy of ER in the space between 0-100nm near the PM (**Figure 3e**), and we encounter 65.71% volume fraction in 0 - 100nm (**Figure 3f**). This is in line with recent findings in the nucleus accumbens where the PM of the neuronal somata of neurons were even found to be covered with ER to a much larger extent than spines, dendrites, and axons (*9*). Since this type of ER in proximity to the PM - also called cortical or subsurface ER - have been shown to have a critical role for intracellular calcium signaling (*30*) and for the replenishment of ER calcium stores (*31*), we went on to measure the ratio of the PM, which is in close proximity to ER. We found that 4.79 % of the PM is covered with subsurface ER withinin 30nm distance in the electron tomogram data. This area fraction is in line with what has been described for the soma of other neuron types (for comparison: 4-12% within 30nm distance in neurons in the nucleus accumbens (*9*)), possibly reflecting the importance of ER-PM contacts for the neuron physiology in Purkinje neuron.

To further improve our understanding if somatic domains exist within the intracellular distribution of the ER, we took advantage of the high-resolution electron tomography (**Figure 3g**) and the ER reconstructions (**Figure 3h**) and performed a density analysis within the Purkinje neuron (**Figure 3i**), which revealed that peaks in the ER density maps are caused by

167 particularly organized structural motifs of the ER (**Figure 3j**), namely layered subsurface ER
168 (**Figure 3k**), ER stacks (**Figure 3l**) and layered ER sheets (**Figure 3m**), which is in line with
169 known ER assemblies (*13*).
170 However, contrary to textbook descriptions of the ER, which often portray an exclusive parallel
171 orientation to the nuclear envelope and cell membrane, we found in all our EM datasets that
172 this parallel orientation is highly intermingled with ER oriented in any other orientation angle
173 towards the PM (**Figure 3n-o**). To determine if these angles are distributed completely at
174 random or if a preferential ER organization exists, we went on to measure the orientation angle
175 of ER strands in the mouse SBEM volume in relation to the plasma membrane as well as in
176 relation to the nuclear envelope. We define the parallel orientation to the plasma membrane
177 as 0º whereas a perpendicular orientation as 90º (**Figure 3p**). While we find a preference
178 towards orientation angles that are nearly parallel to the plasma membrane and nuclear
179 membrane (45.1% of ER strands are within 0˚± 30˚ angle difference between ER and PM), we
180 also find that a large proportion of ER is oriented perpendicular (24.3% within 90˚± 30˚ angle
181 difference between ER and PM) or at any angle between these two extremes (**Figure 3q**). This
182 suggests that outside of the parallel orientation, there is no clear preference for another
183 orientation angle and all configurations occur. Importantly however, we found that the relative
184 frequency at which the preferred orientation (parallel to the PM) occurs is dependent on the
185 PM-ER distance and that the relative frequency of ER perpendicular to the PM increases at
186 larger PM-ER distance (**Figure 3t**), making consistently above 30% at >200nm (mean: 33%
187 between 200-500nm) distance from the PM.

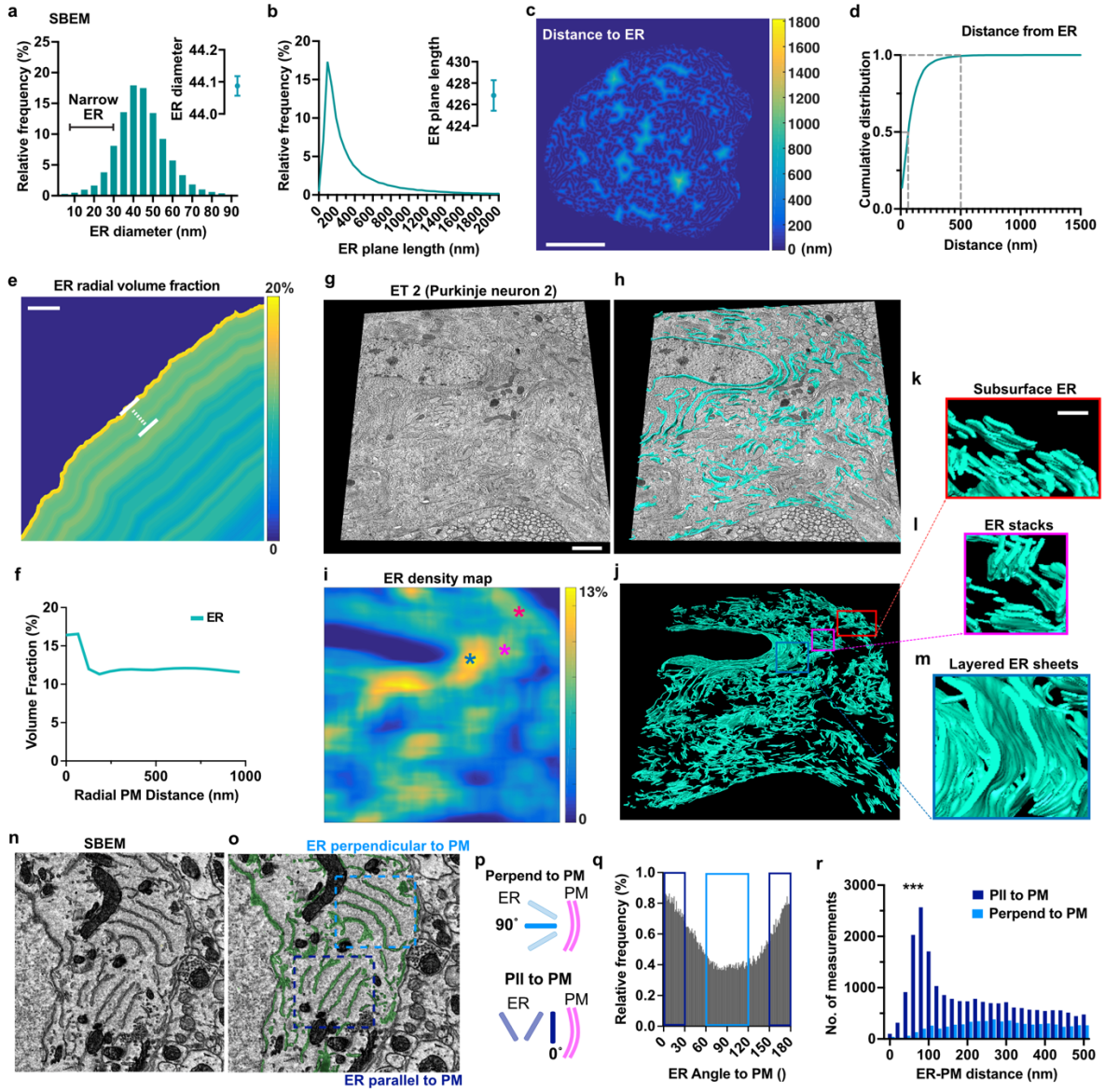


**Figure 3. ER is also oriented perpendicular to the somatic plasma membrane of Purkinje neurons.** Analysis of the ER morphology of the electron tomograms shows (**a**) ER diameter of 39.25 nm ± 10.55 nm (**b**) 426.8 nm ± 580.5 nm 2D plane ER strand length. (**c**) Heatmap plot of ER distance maps, shows if intracellular areas are void of ER (light colors). (**d**) The cumulative ER distance plot across the entire soma of the SBEM reconstruction reveals that the majority (>50%) of the Purkinje neuron soma has ER in close proximity (within 55nm) and almost all the soma (99%) has ER within 500nm. (**e**) The ER radial heat map (of a single example plane) and (**f**) the cumulative radial distribution plot (across the entire soma) display the ER volume fraction of the cell at each distance of the surface and reveal a high content of subsurface ER (within 100nm from the PM). Based on a (**g**) high-resolution electron tomography volume the (**h**) ER segmentations were transformed into (**i**) density maps which reveals that ER density peaks (light colors, yellow) are correlated to the occurrence of structural motifs of the ER, in particular subsurface ER (red label in **i-j**; and m), ER stacks (magenta label in **i-j**; l) and layered ER sheets (blue label in **i-j**; m). (**n-r**) The orientation of ER strands was quantified relative to the PM and (**p-q**) defined as parallel (pll; dark blue) or perpendicular (perpend; light blue) to the PM. (**p**) Exemplified schema of the calculation of the different angles of ER stacks. (**q**) Distribution of ER angle calculated relative to the plasma membrane (PM). (**r**) An overall preference of the ER to orient in parallel to the PM particularly at close distances to the PM is evident (ratio of pll to perpend: 93% to 7%) whereas further away from the PM the fraction of perpendicular ER increases (ratio of pll to perpend: 64% to 36%). Scale Bars (c): 5µm; (e, g-j): 1µm; (k-m): 250nm

## Mitochondria ultrastructure in the Soma of Purkinje neurons

Since the exact distribution and morphologies of mitochondria have important implications for the energy supply of different intracellular domains, and have not been described for Purkinje

192 neurons, we next aimed to perform a detailed characterization of this cellular ultrastructure
193 based on the 3D reconstructions of 2712 mitochondria (**Figure 4a**), with a density of 0.79
194 mitochondria / $\mu m^3$ in the Purkinje neuron soma. Across the mitochondria we found an average
195 diameter of 132 nm ± 1.16 nm (**Figure 4b**) and length of 2533nm ± 566nm (**Figure 4c**) and an
196 average volume of 0.11 $\mu m^3$ ± 0.02 $\mu m^3$ (**Figure 4d**). Since the Mitochondria Complexity Index
197 (MCI) has been found to vary and was implied in ageing, we wanted to test if the MCI is similar
198 across cell types and if it is therefore comparable in Purkinje neurons. The average MCI in our
199 Purkinje neurons was 5.34 ± 0.94 (**Figure 4e**), which is similar to the recently described MCI
200 in hippocampal CA1 and DG cells (*32*). Based on our findings we developed an average shape
201 descriptor (with standard deviation) of somatic mitochondria in the Purkinje cell bodies (**Table**
202 **1**). We further determined the orientation of mitochondria in the tomography volumes and in
203 the SBEM dataset, and found that unlike the ER, that mitochondria have no clear preference
204 to orientate parallel relative to the cell membrane (**Figure 4g-i**). We thus expect that the
205 orientation of the ER may influence the neuron function, not only at the level of the diffusion of
206 signaling molecules but potentially also more directly at the level of Calcium signaling.
207 Unlike for the ER, only about one quarter of the soma is very close to the next mitochondria
208 within 250 nm (28.03% within 250nm), meanwhile 78.33% of the soma is within 500nm of the
209 next mitochondrion (**Figure 4 k-l**). This means that in the Purkinje neuron soma the ER is more
210 dispersed than mitochondria throughout the soma, with effectively every region of the soma
211 containing ER. Thus, compared to the ER, there are somatic areas comparatively far from
212 mitochondria (**Supplementary Figure 3**). Further, we find that areas devoid of mitochondria
213 are often where large stacks of large multi-layered ER sheets are located (**Figure 4m**).
214 We also characterized the radial intracellular distribution of mitochondria, by measuring their
215 relative volume occupancy across the soma with respect to their distance to the PM (**Figure**
216 **4n-q**). We find that in contrast to the ER, mitochondria were mostly present at distances above
217 200nm and more from the PM (**Figure 4r**), and that only few mitochondria are in contact with
218 the somatic plasma membrane. The ER is frequently closely associated with mitochondria,
219 forming regions known generally as ER membrane contact sites (MCSs). It is known that these
220 contact sites of the ER, mitochondria and cell membranes are critical for maintaining the
221 calcium in balance in the soma and facilitate the calcium uptake into the ER and mitochondria
222 (*8*, *33*), which influence mitochondrial function and energy metabolism and are vital for various
223 cellular processes. To better understand the structural organization of ER–mitochondria
224 contact sites, we quantified their radial distribution within the soma, defining contact sites as
225 regions where the ER–mitochondria distance is less than 30 nm. We found a prominent peak
226 in the radial distribution at 250 nm distance from the PM, which is at the intersection point of
227 the radial peaks of ER and mitochondria (**Figure 4r**).

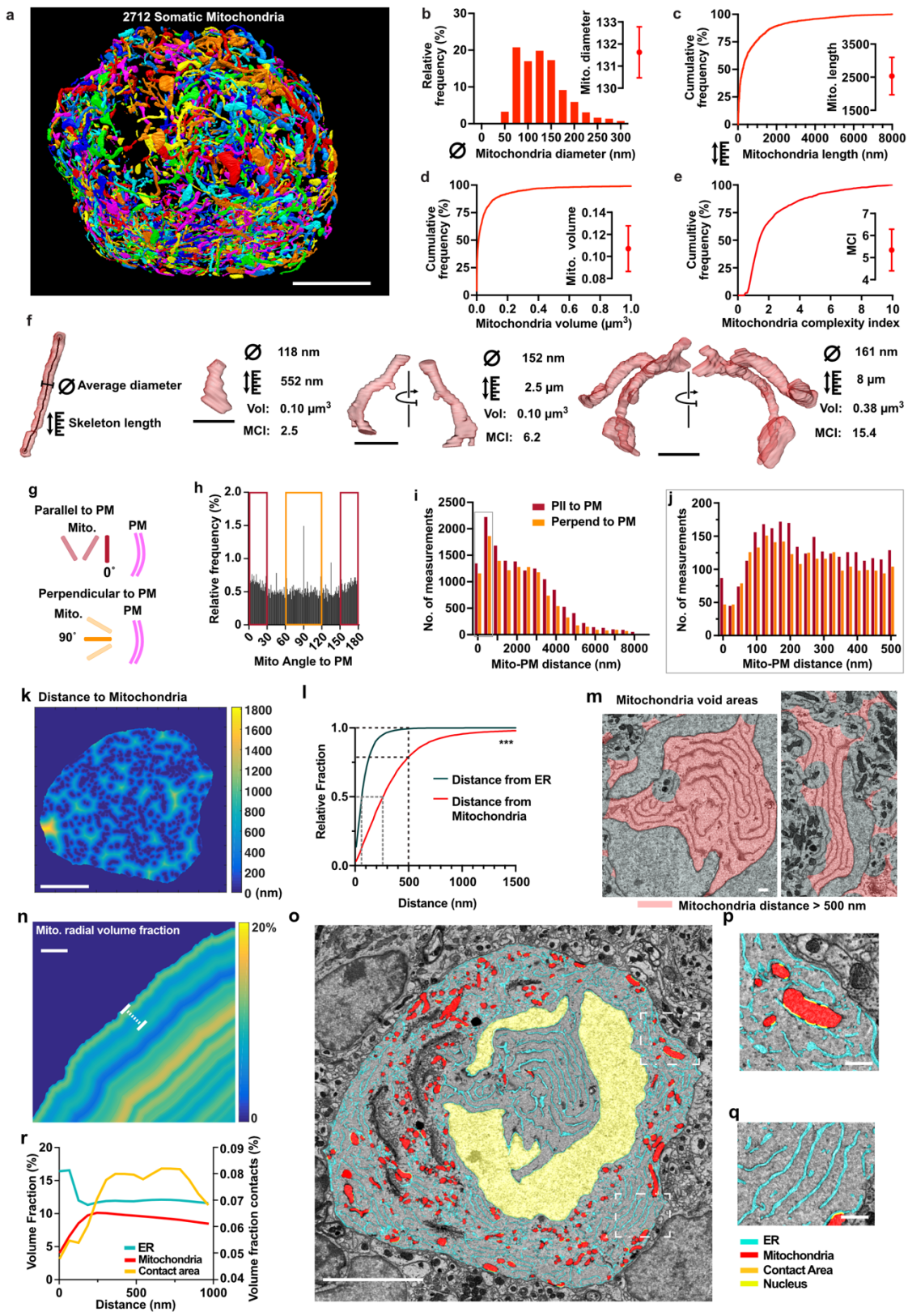


**Figure 4. Mitochondria ultrastructure in the Soma of Purkinje neurons.**
(**a**) 3D color-coded rendering of 2712 mitochondria inside a single Purkinje neuron soma. (**b**) Diameter per mitochondrion (nm). (**c**) Cumulative distribution and average length with SEM of mitochondria. (**d**) Cumulative distribution and average volume with SEM per mitochondrion in µm$^3$. (**e**) Cumulative distribution and average with SEM of the Mitochondria Complexity Index (MCI). (**f**) 3D renderings of representative examples for different types of mitochondria. A skeletonization version is used to determine the length and the mean diameter is determined as the closest distance to the surface at each point of the skeleton. Orientation of mitochondria was quantified relative to the PM and (**g-j**) defined as parallel (pll; red) or perpendicular (perpend; orange) to the PM. (**k**) Heatmap plot of mitochondria distance maps, shows where intracellular areas are void of mitochondria (light

colors). (**l**) The cumulative mitochondria distance plot across the entire soma of the SBEM reconstruction reveals that mitochondria are less distributed than the ER throughout the soma, (**m**) leaving areas of large ER sheets without mitochondria. (**n**) Mito distance maps (**o-q**) example images (**r**) and cumulative radial distribution plot (across the entire soma) reveal that mitochondria are inwards shifted as compared to the ER, with ER-mitochondria contact sites also increasing until 250nm distance from the PM. Scale Bars: (**a,k,o**) 5µm; (**n**) 1µm; (f, p,q) 0.5µm

228

229 **Table 1. Average shape descriptor of somatic mitochondria in the Purkinje neurons**

| | Volume | Length | Diameter | MCI |
|---|---|---|---|---|
| Mean ± S.E.M | 0.11 ± 0.02 $\mu m^3$ | 2533 ± 566nm | 132 ± 1.16 nm | 5.34 ± 0.94 |

230

231 **The mitochondrial and endoplasmic reticulum endoarchitecture from the axon initial**
232 **segment to the first heminode of Ranvier**

233 The axon initial segment (AIS) is a thin, unmyelinated region of the axon that originates from
234 the axon hillock and has a critical role in the neuronal physiology, as it generates action
235 potentials in Purkinje neurons (*34*) and the length axon initial segment was shown to provide
236 an additional mechanism for adjusting neuronal excitability (*35*, *36*). Even though several
237 structural features have been described in the AIS, such as a discrete axoplasmic reticulum
238 (*3*), a rather unique dense granular material coating the interior of the axon membrane (*37*)
239 and disc-like ER structures resembling the spine apparatus (*3*, *38*), which are thought to be
240 increased at proximity to GABAergic projections, our understanding of the overall
241 ultrastructural organization in this zone still remains rudimentary. Since both the ER and
242 mitochondria are storing and releasing intracellular calcium, they play a critical role in this zone
243 for the generation of action potentials (reviewed in (*39*)). To examine the ultrastructure of the
244 AIS in more detail we segmented the cytoplasm (**Figure 5a**), the ER and the mitochondria. We
245 separated the AIS into sub-regions, from the internodal region (**1**), the first heminode of Ranvier
246 with the juxtaparanode (**2**) and hemi-paranode (**3**), the distal (**4**), medial (**5**) and proximal AIS
247 (**6**) and the axon hillock (**7**; **Figure 5b**). Along these subregions we find significant variations
248 in the content of ER and mitochondria (**Figure 5c**). Among those the myelinated axon areas
249 (**1&2**) have a significantly increased content in mitochondria, whereas mitochondria appear
250 almost completely absent from the paranodal region (**3**) and the proximal AIS (**6**) (see **Figure**
251 **5c-d, g-h**). The ER content is however significantly elevated in the narrow paranode and distal
252 AIS, while it is also decreased in the proximal AIS (**Figure 5c-d, e-f, h).** The reduced amount
253 of both, mitochondria and ER in the proximal AIS might be related to the occurrence of the
254 prominently visible microtubule bands in this segment (**Figure 5h**).

255 The first heminode of Ranvier has a critical role for the action potential initiation and for burst
256 firing (*40*). Interestingly, we identify some notable differences at the anatomical level in the
257 axon diameter of Purkinje neurons, which decreases at the heminode, from a mean diameter
258 of 622nm (at the medial AIS) at the unmyelinated axon to 475nm at the paranode before the
259 myelination begins. However, as soon as the myelination begins (at the juxtaparanode) the

260 axon diameter increases to 1000nm (**Figure 5e**) and then continues with a mean diameter of
261 855nm (**Table 2**).
262 Since the ER is continuously very prominent throughout the entire heminodal area, we
263 examined its relative content in more detail, and found it increases punctually in a microdomain
264 at the nodal constriction, making up to 50% of the entire cytosol (**Figure 5f**), whereas it
265 decreases towards the myelinated AIS at the perinode and the juxtaparanode back to below
266 25%. Conversely, the mitochondrial content decreases, and falls to a complete absence at the
267 nodal constriction (**Figure 5g**), whereas moving along further into the juxtaparanode, once the
268 myelination enveloped the axon the mitochondria content increases substantially to 50% and
269 remains elevated at about 25% at the internode region, inside the myelinated axon. We further
270 noted several degradative catabolic organelles in the juxtaparanodal and paranodal region of
271 the AIS.
272

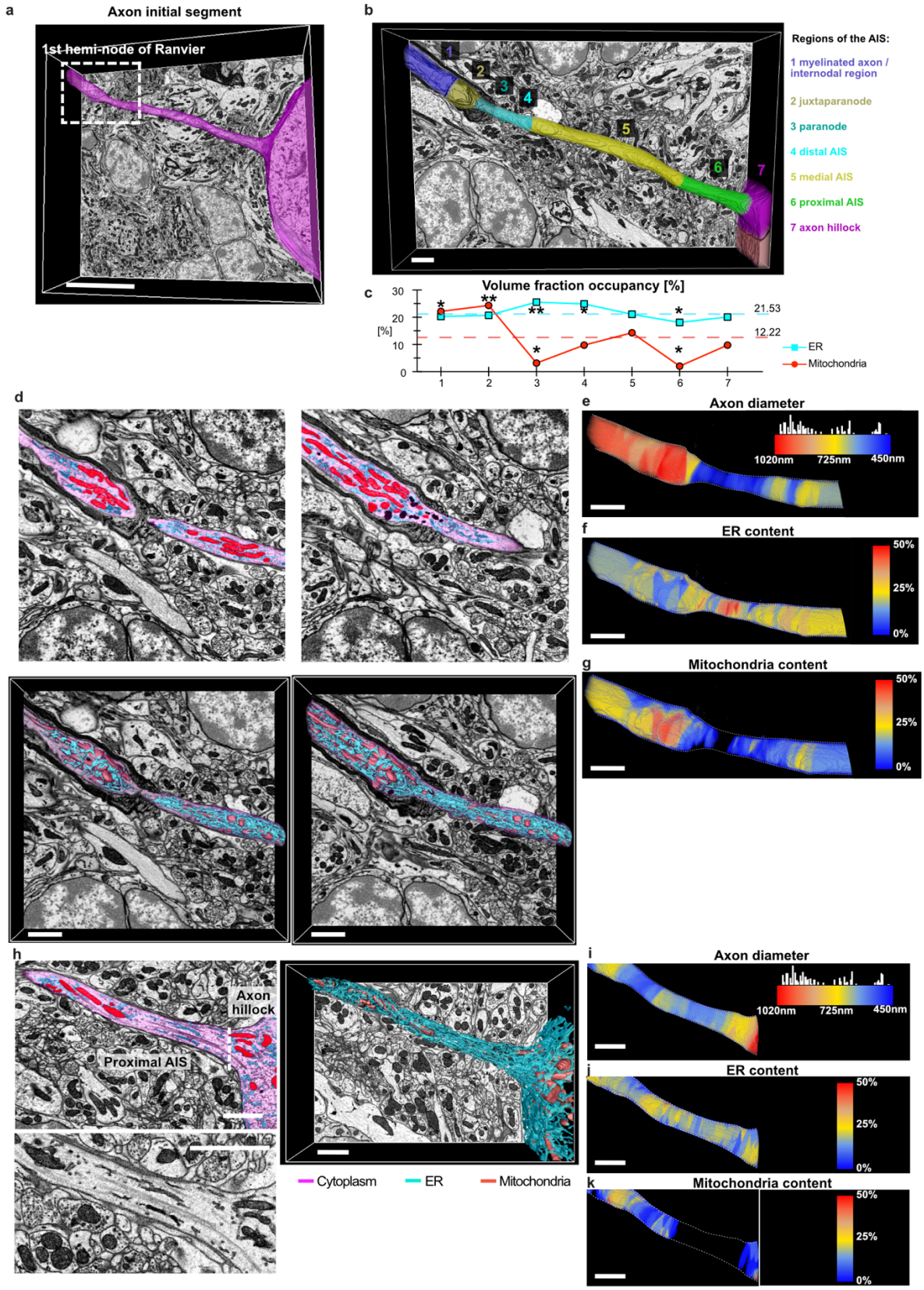


**Figure 5. Intracellular distribution of ER and Mitochondria along the axon initial segment from the axon hillock until the first node of Ranvier. (a)** 3D surface reconstruction of the Axon initial segment (AIS) from a SBEM volume. (**b**) The AIS was further divided into sub-regions to analyze if intracellular differences occur along the AIS. (**c**) Volume occupancy of ER and mitochondria along the subregions of the AIS shows strong variations, with absence of mitochondria in the proximal AIS (6) and close to the heminode (3). The mean contents are represented by dash lines. (**d**) 2D segmentations of sections of the hemi-node and 3D volume rendering shows the transition points at the heminode, with high ER, low mitochondria content. (**e**) Color-coded rendering of the axon diameter shows a narrowing of the axon to 450nm at the hemi-node, with a strong widening to 1µm once

the axon is myelinated. (**f**) Color-coded rendering of the ER content reveals a nanodomain of very high ER-content (up to 50%) at the narrow constriction of the heminode. (**g**) Color-coded rendering of the ER content reveals that in the same nanodomain mitochondria are completely absent. Whereas the juxta-paranode contains elevated levels of mitochondria, which are more than twice the average in the AIS. (**h**) 2D section of the axon hillock and the proximal AIS shows the large microtubule filaments contained in this area. 3D rendering of the ER and mitochondria segmentations shows mostly ER and less mitochondria in the axon towards the hillock. Color-coded rendering (**i**) of the axon diameter displays a broadening of the axon towards the hillock with (**j**) continuous content of ER but (**k**) an absence of mitochondria in the proximal AIS. *: $p<0.05$, **: $p<0.01$ Scale Bars: A: 5µm. B and D-K: 1µm.

**Table 2. Anatomy of the axon initial segment from the axon hillock until the first node of Ranvier**

| **AIS region** | **1 Internode (myelinated)** | **2 Juxta-paranode** | **3 Hemi-(para)node** | **4 Distal AIS** | **5 Medial AIS** | **6 Proximal AIS** | **7 Axon hillock** | **Sum:** | **Mean:** |
|---|---|---|---|---|---|---|---|---|---|
| **Length [µm]** | 1.45 | 0.99 | 0.89 | 1.81 | 6.65 | 2.94 | 2.58 | 17.31 | n.a. |
| **Volume [µm$^3$]** | 2.37 | 1.43 | 0.34 | 0.74 | 4.25 | 1.95 | 3.22 | 16.68 | n.a. |
| **Ø Diameter [nm]** | 857 | 855 | 475 | 534 | 622 | 644 | 505 | n.a. | 603 |

## Discussion

To date our understanding of the intracellular organization of neurons is shaped by long-standing analysis performed on 2D electron microscopy and resolution-limited fluorescence-based 3D light microscopy of selectively stained or fluorescent protein marked molecules or structures. As new techniques now allow imaging of large 3D extents with high resolution volumetric electron microscopy, a major challenge has remained for one to perform the segmentation of these data at the required scale and precision, allowing accurate quantification of details of these distinct intracellular structures and their associations with one another. The second challenge to improve our understanding the vast complexity of the intracellular organization lays in defining features to analyse, which can distil the organization principles out of a seemingly chaotic cytoplasm. As future studies will increasingly aim to understand the *endoarchitecture* within neurons, to know which are organizational principles and how they are physiologically contributing, it is first and foremost important to identify features which can be used to describe this architecture. With this study, we intend to lay out an important path for future studies to examine the organization principles of 3D neuronal ultrastructure in health and disease. Looking ahead, a complete *neuronal endoarchitectome* of adult nervous tissue will require to encompass a broad range of constituents including mitochondria, the ER, the Golgi apparatus, peroxisomes, and lysosomes. Traditionally viewed as purely catabolic organelles, lysosomes are becoming recognized as active participants in regulating anabolic processes, particularly through their interaction with the ER where their positioning was shown to directly influence ER remodeling and tubule dynamics in response to metabolic states (*41*). This highlights a bidirectional communication between degradation pathways and biosynthetic compartments. Incorporating such catabolic-anabolic crosstalk will be important for future

300 studies aiming to understand neurodegenerative diseases. Importantly, since neurons are
301 long-lived and do not divide, it is critical to perform these quantifications of spatially distinct
302 patterns of the neuronal endoarchitectome in adult brain tissue as it has been shown that
303 dynamic reorganizations such as mitochondrial mobility are much reduced in this system as
304 compared to cultured cells or primary neuronal cultures (*42*, *43*).
305 When considering the neuronal energy metabolism, we discovered several interesting features
306 in the distribution of mitochondria. For one, we found several areas of the neuron where
307 mitochondria are absent, and therefore the energy must be supplied e.g. by diffusion of ATP
308 from adjacent areas. While it is common knowledge that mitochondria are absent inside the
309 nucleus, we found that, in addition, mitochondria are often absent from the areas surrounding
310 the nucleus where large ER sheets are present, as well as from certain axonal subregions.
311 Most noteworthy is an absence of mitochondria at the heminodal constriction, the most distal
312 non-myelinated area of the AIS, since this has been identified to be the an area critical for the
313 initiation of both, simple and complex spikes in Purkinje neurons (*44*). $Na^+$ channels at the
314 distal AIS are essential for the generation of action potentials (*45*) and recent studies found
315 that the sodium channels in this area are underlying burst firing (*40*) and that their content in
316 this area regulates the threshold for action potential generation (*46*). After an action potential
317 however, the electrogenic $Na^+/K^+$-ATPase has to be highly active to elevate the membrane
318 potential and to restore the ion gradient again. The absence of mitochondria of the neuron in
319 this area is therefore puzzling, as this process is entirely ATP dependent.
320 Noteworthy is however also the drastic reduction in the axon diameter that we observed, which
321 implies that a substantially smaller number of $Na^+$-ions are required due to the much smaller
322 volume (since a 30% reduction in diameter from the average axonal diameter of 0.6µm to
323 0.45µm already leads to a >50% reduction in axonal volume). It is interesting that in the same
324 axonal nanodomain the ER composes 50% of the axoplasmic volume. We therefore postulate
325 that elevated $Ca^{2+}$ concentrations can occur in this particular nanodomain and that excluding
326 mitochondria from this area prevents exposing them to toxic $Ca^{2+}$ levels which would be a
327 death signal for mitochondria (*47*). At the same time the reduced axonal volume also lowers
328 the amount of ATP required to restore the membrane potential and excitability, making it more
329 energy-efficient overall.
330 Conversely, several regions within the cell exhibit an extremely elevated mitochondrial content.
331 Notably one of the areas with the highest mitochondria content is the juxtaparanode where up
332 to 50% of the axoplasm is occupied by mitochondria, which provides a likely source of ATP to
333 support the $Na^+/K^+$-ATPase activity, which is essential for sustaining to enable repeated action
334 potentials at the first heminode of Ranvier.
335

336 **Methods**

337 All animal procedures were approved by the Institutional Animal Care and Use Committee
338 (IACUC) of University of California, San Diego and complied with all relevant ethical regulations
339 for animal research.

340

341 **Tissue preparation for serial block-face scanning electron microscopy (SBEM) and**
342 **electron tomography**

343

344 Samples for SBEM were prepared as described in (*27*). Male mice and rats (age 4–6 weeks)
345 were anesthetized using a mix of ketamine (Pfizer, 10mg/kg, i.p.) and xylazine (Lloyd, 2mg/kg,
346 i.p.). They were then perfused transcardially first with Ringer's solution at 37°C containing
347 heparin (10 units/ml) for 3 minutes and then perfused for 15 min with a fixation solution
348 containing 2% paraformaldehyde, 2.5% glutaraldehyde and 2 mM CaCl2 in 0.15 M sodium
349 cacodylate buffer. Fixation was initiated at 37 °C and then cooled to 4 °C. The brain was then
350 placed in ice-cold fixative for 2-5 h. Brain sections of the cerebellum were cut parasagittal into
351 100µm thick slices using a vibratome (Leica). The slices were stained with reduced Osmium
352 (2% OsO4/1.5% potassium ferrocyanide) in ice-cold 0.15M cacodylate buffer for 1 h. After
353 washing 3x for 5 min, the slices were placed for 20min in a filtered 1% thiocarbohydrazide
354 (TCH) solution. The slices were rinsed 3x with ddH2O and then placed in 2% OsO4 for 30 min.
355 The sections were rinsed with ddH2O and left in 2% uranyl acetate aqueous solution overnight
356 at 4°C. On the following day, sections were washed 5x 2 min in ddH2O at room temperature.
357 Slices were gradually dehydrated using a series of ice-cold ethanol solutions (50%, 70%, 90%,
358 100%, 100%) for 5 min each. Tissue sections were placed for 10min in ice-cold 100% acetone
359 and 10min in 100% acetone at room temperature. Sections were infiltrated using 50%
360 acetone–50% Durcupan ACM epoxy resin (Electron Microscopy Sciences) mix for 6 hrs. Slices
361 were placed 3x in fresh 100% Durcupan every 6 hrs over the next day. The stained slices were
362 embedded in 100% Durcupan with ACLAR and two mold-release coated glass slides and resin
363 was hardened in vacuum at 60°C for 48 h.
364 Samples for ET were prepared as described as described in (*27*).

365

366 **Image Acquisition**

367 *SBEM acquisition*

368 SBEM was performed using a Merlin SEM (Zeiss) with a Gatan 3View system at high vacuum.
369 The SBEM volume from the cerebellum of a P40 male mouse was acquired with dimensions
370 of 57.17 × 76.22 × 17 $\mu m^3$. The mouse SBEM volume was acquired at 4.76nm x/y pixel spacing
371 and 70nm section thickness. A SBEM volume of 189 × 118 × 60 $\mu m^3$ from a rat sample

372 (5288071) was acquired with 2.6 keV at 5.9nm x/y pixel spacing (1210x Magnification) and
373 40nm section thickness with a raster size of 32.000 x 20.000 pixels.
374
375 *Electron Tomography*
376 Five multi-tilt electron tomograms of semi-thin sections were acquired in the mouse
377 cerebellum, covering each 24.7 - 377.3 $\mu m^3$, from the axonal as well as the dendritic pole of
378 Purkinje neurons at 2.1 nm - 3 nm voxel size with 0.5 degree and reconstructed at 4.2 nm - 6
379 nm voxel size in x/y/z and reconstructed, with following specific parameters. Tomogram 1
380 volume dimensions were 12.9 x 12.9 x 1.06 $\mu m^3$ and the volume was reconstructed at 4.3 nm
381 voxel size in x/y/z. Tomogram 2 volume dimensions were 12 x 12 x 2.62 $\mu m^3$ and the volume
382 was reconstructed at 6 nm voxel size in x/y/z. Tomogram 3 volume dimensions were 12 x 12
383 x 0.44 $\mu m^3$ and the volume was reconstructed at 6 nm voxel size in x/y/z. Tomogram 4 volume
384 dimensions were 8.4 x 8.4 x 0.35 $\mu m^3$ and the volume was reconstructed at 4.2 nm voxel size
385 in x/y/z. Tomogram 5 volume dimensions were 8.4 x 8.4 x 0.69 $\mu m^3$ and the volume was
386 reconstructed at 4.2 nm voxel size in x/y/z.
387
388 **Data analysis**
389 **General workflow and software used**
390 Image segmentation for all cellular organelles consisted of a workflow of initial manual training
391 data generation. Manual image segmentations and manual proof editing was performed using
392 VAST Lite (*48*) or IMOD (*49*). Subsequently CDeep3M (*27*), a software package to train and
393 apply a deep neural network for large-scale image segmentation, was trained on different
394 cellular constituents. Data was computationally segmented and manually proof-edited.
395 Subsequent data analysis and quantifications were performed in Matlab and in Python. Data
396 rendering was performed in Amira 3D (2023.1.1). Statistical analysis and plotting of graphs
397 were performed in GraphPad Prism. Figures were assembled in Affinity Designer (1.10.8).
398
399 **Volume occupancies**
400 Volume occupancies of subcellular organelles were computed per image plane by quantifying
401 the number of segmented pixels for each structure relative to the total soma volume. The
402 fractional occupancy of mitochondria, endoplasmic reticulum, Golgi apparatus, and nucleus
403 was expressed as a percentage of soma area in each plane, and converted to physical volume
404 using known voxel dimensions, with cytoplasmic volume inferred by subtraction.
405
406 **Morphometric Analysis of the endoplasmic reticulum**
407 Endoplasmic reticulum (ER) morphology was quantified on a per-plane basis using 2D
408 segmentations. Each ER structure within a plane was identified as a distinct connected region

409 and analyzed individually. For each ER strand, a skeleton representation was computed to
410 identify its central axis. To assess the relative orientation of the ER with respect to the plasma
411 membrane (PM), the angle of the central axis of each ER strand was calculated, along with
412 the angle of the PM curvature at the point closest to the ER. The ER strand length was
413 calculated by summing the pixels along its skeleton and converting the result into micrometers
414 using the pixel dimension. To estimate the diameter, a 2D distance transform was applied to
415 the ER segmentation, and local radii were sampled along the entire skeleton path; the mean
416 diameter was calculated as the average of doubled distance transform values at each skeleton
417 point. To assess the proximity of the cytoplasm to the next ER (or mitochondria) a distance
418 map was computed from the inverse image within the soma mask. Occurring distance values
419 were concatenated across the entire cell for the ER and for mitochondria to identify the
420 aggregated distance within the cell to the most proximate ER or mitochondrion.
421
422 **Mitochondrial 3D Morphometry Analysis**
423 To assess the 3D morphology of individual mitochondria in SBEM (serial block-face electron
424 microscopy) datasets, segmented binary volumes of mitochondria were analyzed using voxel-
425 based and mesh-based geometric descriptors. First isolated mitochondria were isotrapically
426 resampled and 3D skeletonization was applied to each mitochondrial volume to extract its
427 medial axis. The total mitochondrial length was then estimated by summing the number of
428 skeleton voxels and converting to micrometers using the voxel dimensions. To estimate the
429 diameter, a 3D distance transform was applied to the mitochondrial volume, and local radii
430 were sampled along the entire skeleton path; the mean diameter was calculated as the
431 average of doubled distance transform values at each skeleton voxels. Mitochondrial volume
432 was quantified using two approaches: voxel-based volume (via simple voxel counting) and
433 mesh-based volume (via triangulated isosurface calculation).
434 The Mitochondria complexity index was calculated as described earlier (*50*) as metric to
435 distinguish morphologically complex from simple mitochondria using following formula:
436 $\mathrm{MCI} = \frac{\mathrm{SA}^3}{16\pi^2\mathrm{V}^2}$ where SA is surface area and V is volume.
437
438 **Plasma Membrane Coverage Analysis**
439 In the electron tomography volumes, we quantified the coverage of the plasma membrane
440 (PM) by the endoplasmic reticulum (ER). To this end we performed a 2D plane-wise analysis
441 on binarized segmentation masks of the soma and ER. The PM was defined as the perimeter
442 of the soma mask, extracted using morphological edge detection. To avoid misclassification at
443 the edge of the tomogram, pixels close to the image borders were excluded from the PM
444 analysis. For each PM pixel, the Euclidean distance to the nearest ER-positive pixel was
445 computed using a distance transform. A PM pixel was considered “covered” by ER if it was

located within 30 nm of any ER signal, based on the in-plane pixel resolution provided for the dataset. The percentage of covered PM pixels was calculated for each plane, and results were aggregated across the full image stack.

**3D axon diameter map**

To color code the axon segmentation for the axon diameter we developed following strategy: The image stack with the binary axon segmentation was isotropically re-sampled to 36nm (or 18nm) voxelsize, and a skeletonization as well as the inverse directed 3D distance transform were calculated from the isotropic image stack. The diameter at each point of the binary skeleton is twice the 3D distance transform. Therefore, the skeleton was multiplied with 2x the 3D distance transform, multiplied by the resampled voxelsize (36nm), which results in a 3D skeleton encoding the axon diameter at each centerpoint of the axon. To revert the diameter of the axon to its 3D extent we calculated the index map of the closest point on the skeleton for the entire axon. Each point of the axon was then reassigned with the value of the closest point on the 3D skeleton encoding the axon diameter. The result is a 3D axon diameter map, which was subsequently volume rendered in Amira (displayed in **Figure 5**).

**3D axonal mitochondria and ER content maps**

As outlined above for the axon diameter map, we also encoded the content of mitochondria and ER. To this end we calculated in a similar manner for each voxel of the axon the closest voxel on the 3D skeleton, and the percent of the axonal voxels belonging (being closest) to each skeleton voxel containing mitochondria or ER respectively. The resulting maps encode the content of mitochondria or ER along the axon (shown in **Figure 5**).

**3D axonal volume fraction content**

The volume fractions across the different regions of the AIS were calculated by dividing voxels that are mitochondria or ER in the region by the total voxels in this region. One sample t test was used to compare segments to the population mean using GraphPad Prism.

**References**


1. M. L. Watson, THE NUCLEAR ENVELOPE. *The Journal of Cell Biology* **1**, 257–270 (1955).

2. M. P. Henkart, T. S. Reese, F. J. Brinley, Endoplasmic Reticulum Sequesters Calcium in the Squid Giant Axon. *Science* **202**, 1300–1303 (1978).

3. J. Lindsey, M. Ellisman, The neuronal endomembrane system. III. The origins of the axoplasmic reticulum and discrete axonal cisternae at the axon hillock. *J. Neurosci.* **5**, 3135–3144 (1985).

484 4. J. De Juan-Sanz, G. T. Holt, E. R. Schreiter, F. De Juan, D. S. Kim, T. A. Ryan, Axonal
485 Endoplasmic Reticulum Ca2+ Content Controls Release Probability in CNS Nerve
486 Terminals. *Neuron* **93**, 867-881.e6 (2017).

487 5. M. Martone, Y. Zhang, V. Simpliciano, B. Carragher, M. Ellisman, Three-dimensional
488 visualization of the smooth endoplasmic reticulum in Purkinje cell dendrites. *J. Neurosci.*
489 **13**, 4636–4646 (1993).

490 6. J. Spacek, K. M. Harris, Three-Dimensional Organization of Smooth Endoplasmic
491 Reticulum in Hippocampal CA1 Dendrites and Dendritic Spines of the Immature and
492 Mature Rat. *J. Neurosci.* **17**, 190–203 (1997).

493 7. J. Lindsey, M. Ellisman, The neuronal endomembrane system. I. Direct links between
494 rough endoplasmic reticulum and the cis element of the Golgi apparatus. *J. Neurosci.* **5**,
495 3111–3123 (1985).

496 8. H. Wu, P. Carvalho, G. K. Voeltz, Here, there, and everywhere: The importance of ER
497 membrane contact sites. *Science* **361**, eaan5835 (2018).

498 9. Y. Wu, C. Whiteus, C. S. Xu, K. J. Hayworth, R. J. Weinberg, H. F. Hess, P. De Camilli,
499 Contacts between the endoplasmic reticulum and other membranes in neurons. *Proc*
500 *Natl Acad Sci USA* **114**, E4859–E4867 (2017).

501 10. M. J. Berridge, Neuronal Calcium Signaling. *Neuron* **21**, 13–26 (1998).

502 11. A. Perez-Alvarez, S. Yin, C. Schulze, J. A. Hammer, W. Wagner, T. G. Oertner,
503 Endoplasmic reticulum visits highly active spines and prevents runaway potentiation of
504 synapses. *Nat Commun* **11**, 5083 (2020).

505 12. Y. Chen, B. L. Sabatini, Signaling in dendritic spines and spine microdomains. *Current*
506 *Opinion in Neurobiology* **22**, 389–396 (2012).

507 13. L. M. Westrate, J. E. Lee, W. A. Prinz, G. K. Voeltz, Form Follows Function: The
508 Importance of Endoplasmic Reticulum Shape. *Annu. Rev. Biochem.* **84**, 791–811 (2015).

509 14. J. Nixon-Abell, C. J. Obara, A. V. Weigel, D. Li, W. R. Legant, C. S. Xu, H. A. Pasolli, K.
510 Harvey, H. F. Hess, E. Betzig, C. Blackstone, J. Lippincott-Schwartz, Increased
511 spatiotemporal resolution reveals highly dynamic dense tubular matrices in the peripheral
512 ER. *Science* **354**, aaf3928–aaf3928 (2016).

513 15. G. J. Augustine, F. Santamaria, K. Tanaka, Local Calcium Signaling in Neurons. *Neuron*
514 **40**, 331–346 (2003).

515 16. W. Denk, H. Horstmann, Serial Block-Face Scanning Electron Microscopy to Reconstruct
516 Three-Dimensional Tissue Nanostructure. *PLoS Biol* **2**, e329 (2004).

517 17. M. Ito, Cerebellar circuitry as a neuronal machine. *Progress in Neurobiology* **78**, 272–303
518 (2006).

519 18. S. Loomba, J. Straehle, V. Gangadharan, N. Heike, A. Khalifa, A. Motta, N. Ju, M.
520 Sievers, J. Gempt, H. S. Meyer, M. Helmstaedter, Connectomic comparison of mouse
521 and human cortex. *Science* **377**, eabo0924 (2022).

522 19. A. Matsliah, S. Yu, K. Kruk, D. Bland, A. T. Burke, J. Gager, J. Hebditch, B. Silverman, K.
523 P. Willie, R. Willie, M. Sorek, A. R. Sterling, E. Kind, D. Garner, G. Sancer, M. F. Wernet,
524 S. S. Kim, M. Murthy, H. S. Seung, The FlyWire Consortium, C. David, J. Joroff, A.
525 Kristiansen, T. Stocks, A. Braun, M. Silies, J. Skelton, T. R. Aiken, M. Ioannidou, M.

Collie, G. A. Linneweber, S. Molina-Obando, S. Dorkenwald, N. Panes, A. M. Gogo, D. Rastgarmoghaddam, C. Pilapil, R. A. Candilada, N. Serafetinidis, W.-C. Lee, A. Borst, R. I. Wilson, P. Schlegel, G. S. X. E. Jefferis, Neuronal parts list and wiring diagram for a visual system. *Nature* **634**, 166–180 (2024).

20. C. M. Schneider-Mizell, A. L. Bodor, D. Brittain, J. Buchanan, D. J. Bumbarger, L. Elabbady, C. Gamlin, D. Kapner, S. Kinn, G. Mahalingam, S. Seshamani, S. Suckow, M. Takeno, R. Torres, W. Yin, S. Dorkenwald, J. A. Bae, M. A. Castro, A. Halageri, Z. Jia, C. Jordan, N. Kemnitz, K. Lee, K. Li, R. Lu, T. Macrina, E. Mitchell, S. S. Mondal, S. Mu, B. Nehoran, S. Popovych, W. Silversmith, N. L. Turner, W. Wong, J. Wu, J. Reimer, A. S. Tolias, H. S. Seung, R. C. Reid, F. Collman, N. M. Da Costa, Inhibitory specificity from a connectomic census of mouse visual cortex. *Nature* **640**, 448–458 (2025).

21. E. Grasso, M. Corteze, H. Schmidt, Connectomic traces of Hebbian plasticity in the entorhinal-hippocampal system. *bioRxiv*, doi: 10.1101/2025.04.07.647631 (2025).

22. A. Shapson-Coe, M. Januszewski, D. R. Berger, A. Pope, Y. Wu, T. Blakely, R. L. Schalek, P. H. Li, S. Wang, J. Maitin-Shepard, N. Karlupia, S. Dorkenwald, E. Sjostedt, L. Leavitt, D. Lee, J. Troidl, F. Collman, L. Bailey, A. Fitzmaurice, R. Kar, B. Field, H. Wu, J. Wagner-Carena, D. Aley, J. Lau, Z. Lin, D. Wei, H. Pfister, A. Peleg, V. Jain, J. W. Lichtman, A petavoxel fragment of human cerebral cortex reconstructed at nanoscale resolution. *Science* **384**, eadk4858 (2024).

23. Z. Zheng, J. S. Lauritzen, E. Perlman, C. G. Robinson, M. Nichols, D. Milkie, O. Torrens, J. Price, C. B. Fisher, N. Sharifi, S. A. Calle-Schuler, L. Kmecova, I. J. Ali, B. Karsh, E. T. Trautman, J. A. Bogovic, P. Hanslovsky, G. S. X. E. Jefferis, M. Kazhdan, K. Khairy, S. Saalfeld, R. D. Fetter, D. D. Bock, A Complete Electron Microscopy Volume of the Brain of Adult Drosophila melanogaster. *Cell* **174**, 730-743.e22 (2018).

24. C. S. Xu, S. Pang, G. Shtengel, A. Müller, A. T. Ritter, H. K. Hoffman, S. Takemura, Z. Lu, H. A. Pasolli, N. Iyer, J. Chung, D. Bennett, A. V. Weigel, M. Freeman, S. B. Van Engelenburg, T. C. Walther, R. V. Farese, J. Lippincott-Schwartz, I. Mellman, M. Solimena, H. F. Hess, An open-access volume electron microscopy atlas of whole cells and tissues. *Nature* **599**, 147–151 (2021).

25. A. Müller, D. Schmidt, C. S. Xu, S. Pang, J. V. D'Costa, S. Kretschmar, C. Münster, T. Kurth, F. Jug, M. Weigert, H. F. Hess, M. Solimena, 3D FIB-SEM reconstruction of microtubule–organelle interaction in whole primary mouse β cells. *Journal of Cell Biology* **220**, e202010039 (2021).

26. L. Heinrich, D. Bennett, D. Ackerman, W. Park, J. Bogovic, N. Eckstein, A. Petruncio, J. Clements, S. Pang, C. S. Xu, J. Funke, W. Korff, H. F. Hess, J. Lippincott-Schwartz, S. Saalfeld, A. V. Weigel, COSEM Project Team, R. Ali, R. Arruda, R. Bahtra, D. Nguyen, Whole-cell organelle segmentation in volume electron microscopy. *Nature* **599**, 141–146 (2021).

27. M. G. Haberl, C. Churas, L. Tindall, D. Boassa, S. Phan, E. A. Bushong, M. Madany, R. Akay, T. J. Deerinck, S. T. Peltier, M. H. Ellisman, CDeep3M—Plug-and-Play cloud-based deep learning for image segmentation. *Nat Methods* **15**, 677–680 (2018).

28. A. T. Kuan, S. Phan, K.-Y. Kim, M. Mackey, M. Kim, S. T. Peltier, M. Ellisman, W.-C. A. Lee, Scalable electron tomography for connectomics. [Preprint] (2024). https://doi.org/10.1101/2024.06.05.597487.

29. M. Terasaki, Axonal endoplasmic reticulum is very narrow. *Journal of Cell Science*, jcs.210450 (2018).

572 30. L. Benedetti, R. Fan, A. V. Weigel, A. S. Moore, P. R. Houlihan, M. Kittisopikul, G. Park,
573 A. Petruncio, P. M. Hubbard, S. Pang, C. S. Xu, H. F. Hess, S. Saalfeld, V. Rangaraju, D.
574 E. Clapham, P. De Camilli, T. A. Ryan, J. Lippincott-Schwartz, Periodic ER-plasma
575 membrane junctions support long-range Ca2+ signal integration in dendrites. *Cell* **188**,
576 484-500.e22 (2025).

577 31. C. Y. Park, P. J. Hoover, F. M. Mullins, P. Bachhawat, E. D. Covington, S. Raunser, T.
578 Walz, K. C. Garcia, R. E. Dolmetsch, R. S. Lewis, STIM1 Clusters and Activates CRAC
579 Channels via Direct Binding of a Cytosolic Domain to Orai1. *Cell* **136**, 876–890 (2009).

580 32. J. Faitg, C. Lacefield, T. Davey, K. White, R. Laws, S. Kosmidis, A. K. Reeve, E. R.
581 Kandel, A. E. Vincent, M. Picard, 3D neuronal mitochondrial morphology in axons,
582 dendrites, and somata of the aging mouse hippocampus. *Cell Reports* **36**, 109509
583 (2021).

584 33. C. Giorgi, S. Marchi, P. Pinton, The machineries, regulation and cellular functions of
585 mitochondrial calcium. *Nat Rev Mol Cell Biol* **19**, 713–730 (2018).

586 34. A. Foust, M. Popovic, D. Zecevic, D. A. McCormick, Action Potentials Initiate in the Axon
587 Initial Segment and Propagate through Axon Collaterals Reliably in Cerebellar Purkinje
588 Neurons. *J. Neurosci.* **30**, 6891–6902 (2010).

589 35. H. Kuba, Y. Oichi, H. Ohmori, Presynaptic activity regulates Na+ channel distribution at
590 the axon initial segment. *Nature* **465**, 1075–1078 (2010).

591 36. M. S. Grubb, J. Burrone, Activity-dependent relocation of the axon initial segment fine-
592 tunes neuronal excitability. *Nature* **465**, 1070–1074 (2010).

593 37. S. L. Palay, C. Sotelo, A. Peters, P. M. Orkand, THE AXON HILLOCK AND THE INITIAL
594 SEGMENT. *The Journal of Cell Biology* **38**, 193–201 (1968).

595 38. T. Kosaka, The axon initial segment as a synaptic site: Ultrastructure and synaptology of
596 the initial segment of the pyramidal cell in the rat hippocampus (CA3 region). *J*
597 *Neurocytol* **9**, 861–882 (1980).

598 39. M. H. P. Kole, G. J. Stuart, Signal Processing in the Axon Initial Segment. *Neuron* **73**,
599 235–247 (2012).

600 40. M. H. P. Kole, First Node of Ranvier Facilitates High-Frequency Burst Encoding. *Neuron*
601 **71**, 671–682 (2011).

602 41. M. Lu, F. W. Van Tartwijk, J. Q. Lin, W. Nijenhuis, P. Parutto, M. Fantham, C. N.
603 Christensen, E. Avezov, C. E. Holt, A. Tunnacliffe, D. Holcman, L. Kapitein, G. S. K.
604 Schierle, C. F. Kaminski, The structure and global distribution of the endoplasmic
605 reticulum network are actively regulated by lysosomes. *Sci. Adv.* **6**, eabc7209 (2020).

606 42. L. Smit-Rigter, R. Rajendran, C. A. P. Silva, L. Spierenburg, F. Groeneweg, E. M.
607 Ruimschotel, D. van Versendaal, C. van der Togt, U. T. Eysel, J. A. Heimel, C. Lohmann,
608 C. N. Levelt, Mitochondrial Dynamics in Visual Cortex Are Limited In Vivo and Not
609 Affected by Axonal Structural Plasticity. *Current Biology* **26**, 2609–2616 (2016).

610 43. T. L. Lewis, G. F. Turi, S.-K. Kwon, A. Losonczy, F. Polleux, Progressive Decrease of
611 Mitochondrial Motility during Maturation of Cortical Axons In Vitro and In Vivo. *Current*
612 *Biology* **26**, 2602–2608 (2016).

44. L. M. Palmer, B. A. Clark, J. Gründemann, A. Roth, G. J. Stuart, M. Häusser, RAPID REPORT: Initiation of simple and complex spikes in cerebellar Purkinje cells: Action potential initiation in Purkinje cells. *The Journal of Physiology* **588**, 1709–1717 (2010).

45. S. Poliak, E. Peles, The local differentiation of myelinated axons at nodes of Ranvier. *Nat Rev Neurosci* **4**, 968–980 (2003).

46. A. Fréal, N. Jamann, J. Ten Bos, J. Jansen, N. Petersen, T. Ligthart, C. C. Hoogenraad, M. H. P. Kole, Sodium channel endocytosis drives axon initial segment plasticity. *Sci. Adv.* **9**, eadf3885 (2023).

47. M. J. Berridge, M. D. Bootman, P. Lipp, Calcium - a life and death signal. *Nature* **395**, 645–648 (1998).

48. D. R. Berger, H. S. Seung, J. W. Lichtman, VAST (Volume Annotation and Segmentation Tool): Efficient Manual and Semi-Automatic Labeling of Large 3D Image Stacks. *Front. Neural Circuits* **12**, 88 (2018).

49. J. R. Kremer, D. N. Mastronarde, J. R. McIntosh, Computer visualization of three-dimensional image data using IMOD. *J Struct Biol* **116**, 71–76 (1996).

50. A. E. Vincent, K. White, T. Davey, J. Philips, R. T. Ogden, C. Lawless, C. Warren, M. G. Hall, Y. S. Ng, G. Falkous, T. Holden, D. Deehan, R. W. Taylor, D. M. Turnbull, M. Picard, Quantitative 3D Mapping of the Human Skeletal Muscle Mitochondrial Network. *Cell Reports* **26**, 996-1009.e4 (2019).

**Authors' contributions**

MGH and MHE conceived and guided the work. MGH, SP, TD and EB performed experiments. MGH performed computational segmentations. MGH, SVS, EPC, KR, YW, LM, BLB performed manual proof-editing of computational segmented data. MGH wrote code to perform computational analysis of the data, did the meshing, rendering and assembly of the figures and drafted the manuscript. All authors read, edited and approved the final manuscript.

**Acknowledgements**

This work was supported by grants from the NIH's NIGMS (R01GM082949) and NINDS/BRAIN Initiative (U24NS120055) and the NSF (2014862) to MHE. This work was supported by a Visible Molecular Cell Consortium (VMCC) fellowship to MGH. This study was further supported by the German Research Foundation (Deutsche Forschungsgemeinschaft; DFG) project ID 509099330 to MGH and SVS and funding from Germany's Excellence Strategy-Exc-2049-390688087 and the DZNE e.V. to SVS.

**Competing interests**

The authors declare that they have no competing interests.

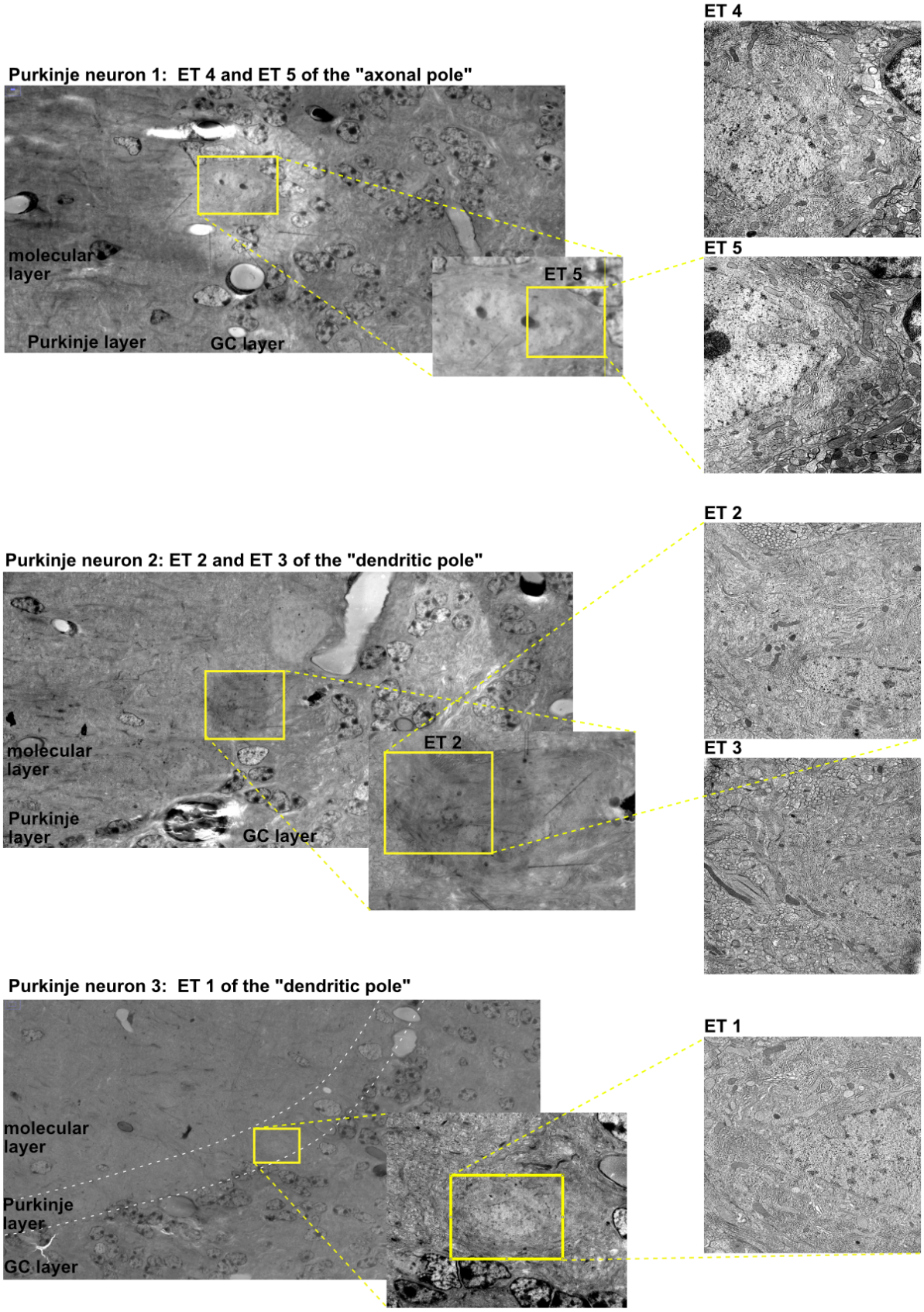


**Supplementary Figure 1. Cerebellar region overview for electron tomography volumes.** Electron tomography volumes were acquired from the dendritic or axonal pole of different Purkinje neurons.

654

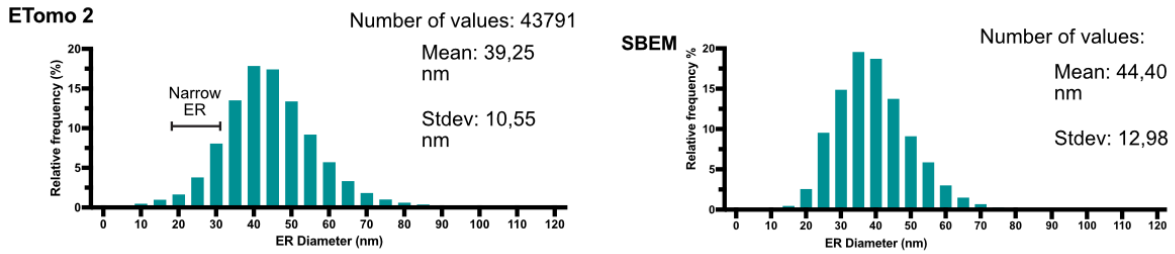


**Supplementary Figure 2. ER diameter quantification using high-pressure frozen freeze substituted electron tomography and chemically fixed SBEM.**

655

656

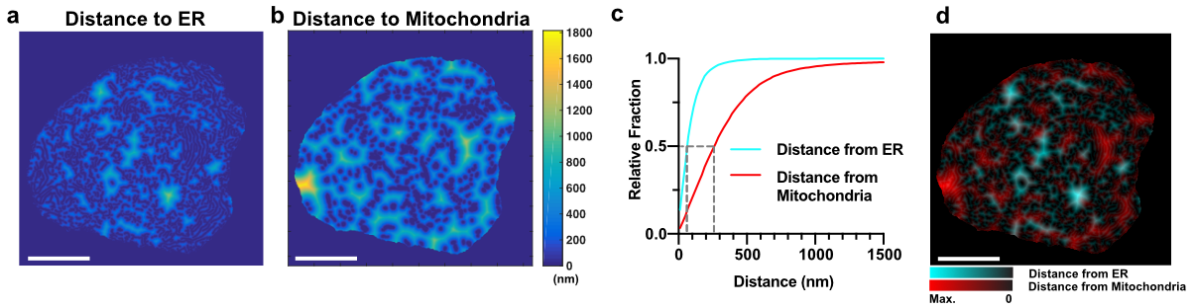


**Supplementary Figure 3. Comparative examination of ER and Mitochondria void areas in the Purkinje neuron soma.** To identify the proximity of the entire soma to the closest mitochondrion and the closest ER we calculated a closest proximity distance map of (a) ER and (b) Mitochondria. (c) The cumulative distance from the closest ER and mitochondria reveals a significantly closer proximity to the ER than to the Mitochondria (Kolmogorov-Smirnov test; $p<0.0001$), where 50% of the soma has ER within 60 nm distance, and 50% of the soma has mitochondrion within 250 nm distance. (d) Overlaying the distance maps of both showed that there is little to no overlap between the areas that are very distant from ER and the areas that are very distant from Mitochondria. Scale Bars: 5μm

657